J. Fluid Mech. (2011), *vol.* 681, *pp.* 173–192. © Cambridge University Press 2011
doi:10.1017/jfm.2011.187

Large-amplitude topographic waves in 2D stratified flow

DAVID J. MURAKI†

Department of Mathematics, Simon Fraser University, Burnaby, BC V5A 1S6, Canada

(Received 15 July 2010; revised 19 January 2011; accepted 17 April 2011;
first published online 16 June 2011)

Our fundamental understanding of steady, stratified flow over two-dimensional (2D) topography rests on the pioneering works of G. Lyra and R. Long. Within linear theory, Lyra established the far-field radiation conditions that determine the downstream pattern of buoyancy waves. Soon after, Long discovered that the steady, nonlinear streamfunction for special cases of stratified, 2D flow could satisfy the same equations as linear theory, subject to an exact topographic boundary condition. Fourier methods are currently used to compute solutions to Long's theory for arbitrary topography in the near-hydrostatic or small-amplitude topographic parameter regimes. It is not generally appreciated however, that these methods encounter difficulties for flows that are both strongly non-hydrostatic and beyond linear amplitudes. By recasting Long's theory into a linear integral equation, this difficulty is shown to be a computational barrier associated with an ill-conditioning of the Fourier method. The problem is overcome through the development of a boundary integral computation which relies on some lesser known solutions from Lyra's original analysis. This method is well-conditioned for strongly non-hydrostatic flows, and is used to extend the exploration of critical overturning flows over Gaussian and bell-shaped ridges. These results indicate that the critical value of the non-dimensional height ($\mathscr{N}\mathscr{H}/\mathscr{U}$) asymptotes to a finite value with increasing non-hydrostatic parameter ($\mathscr{U}/\mathscr{N}\mathscr{L}$).

Key words: internal waves, stratified flows, topographic effects,

1. Introduction

Linear theories for stratified flow over topography were first established during the 1940s with the pioneering works of Lyra (1940), Queney (1948) and Scorer (1949). The first significant theory to address nonlinearity occurred soon thereafter, when Long (1953) noted that the steady theory for stratified flow over two-dimensional (2D) topography could be exactly expressed as a single equation for the streamfunction. Furthermore, conditions of uniform upstream wind and constant density stratification (under a Boussinesq assumption) represented a remarkable special case where the theory reduced to the linear Helmholtz equation. Subsequent laboratory experiments by Long (1955) himself confirmed that this streamfunction theory could accurately predict flows for topography of finite amplitude – including those approaching the point of overturning streamlines. An historical review of early advances using Long's theory, as well as a critical appraisal of its practical limitations, are contained in

† Email address for correspondence: muraki@sfu.ca

https://doi.org/10.1017/jfm.2011.187 Published online by Cambridge University Press

Smith (1979). As a further historical aside, Brown & Christie (1998) cite the very early appearance of the non-Boussinesq version of the streamfunction theory in Dubreil-Jacotin (1937) in the context of surface water waves, rather than the topographic flow problem. (Her original fluid mechanical derivations are found in Dubreil-Jacotin 1932, 1935.) Both for its mathematical simplicity and its broad range of validity, Long's theory represents an important benchmark in our understanding of the nonlinear flow of a stratified fluid over topography.

An important, but subtle issue is how nonlinearity resides within Long's steady streamfunction even though both Lyra's and Long's theories satisfy the same Helmholtz equation at every point in the flow. The entire difference lies within the topographic boundary condition. Long's theory for finite height topography requires the surface to be an exact streamline, and therefore the streamfunction is constant everywhere along a *terrain-following* lower boundary. Linear theory assumes that the topographic height, $\mathscr{H}$, is significantly smaller than the vertical wave scale, $\mathscr{U}/\mathscr{N}$, based on the upstream wind $\mathscr{U}$ and stratification $\mathscr{N}$. Consistent with this is the approximation of the topographic condition by an equivalent vertical motion or buoyancy disturbance at a *flat* lower boundary. As a result, the topographic surface is only approximately a streamline, up to the assumptions of small height terrain.

For atmospheric flows which are assumed to be unbounded above, an upper boundary condition is also required. In classical acoustic and electromagnetic scattering, the theory of the Helmholtz equation with its (radially outward) Sommerfeld radiation condition was already well-understood. However, the far-field corresponding to the upstream/downstream asymmetry of topographic flows represented a significant departure from the standard literature. This issue was not addressed by Long, as his flow experiments and supporting theory were conducted in channels of finite height (Long 1955). However, conditions in the far-field had already been addressed analytically by Lyra (1943) through the imposition of maximal decay of waves upstream. As this upstream decay principle must also apply to Long's theory, nonlinear effects can only be manifested through the finite-height topographic boundary condition.

The earliest realistic depictions of a Long's theory flow in an unbounded atmosphere were the streamlines over a semi-circular obstacle by Kozhevnikov (1968) and Miles (1968). Both works relied upon the representation of Helmholtz solutions as series involving Bessel functions. (Note: the English-language translation of Kozhevnikov 1968 has erroneous notation for the Bessel functions, where formulas containing $I_n(\cdot)$ should appear as $J_n(\cdot)$.) Low-order truncations were then computed to obtain steady (non-hydrostatic) streamline patterns. The precedence for the utility of Bessel series, however, had already been established through the derivation of a Green's function appropriate for Long's theory by Lyra (1943).

An alternative approach to Long's theory involves the use of integral equations. Miles & Huppert (1969) derived scattering and drag formulas for the hydrostatic limit in terms of integral equations involving a Hilbert transform. Streamlines for the hydrostatic flow were produced in Lilly & Klemp (1979) whose computations were based upon a hydrostatic integral equation of Drazin & Su (1975). Moreover, their results were directly verified with the steady state obtained from a time-dependent primitive equation model. The hydrostatic integral equation also formed the basis for the more recent work by Kantzios & Akylas (1993). Predating these, however, were the non-hydrostatic flows obtained by Raymond (1972), from a Fourier-based integral equation solved by iteration. A variation of this Fourier iteration was more recently used by Laprise & Peltier (1989) in their systematic exploration of non-hydrostatic

https://doi.org/10.1017/jfm.2011.187 Published online by Cambridge University Press

flows, and by Durran (1992) for large-amplitude topography in two-layer hydrostatic flows.

In this article, the integral equation methodology is developed to a fuller degree, which exploits both the existing Fourier and Bessel paradigms. In particular, with the increased capacity of computing, accurate solutions to integral equations are obtained by solving large matrix systems. It is first demonstrated that solutions to Long's theory can be directly computed without the need for iterative calculations. Next, it is shown that the usual Fourier methods are ill-conditioned for flows that are sufficiently non-hydrostatic and nonlinear. This numerical limitation is overcome by eschewing the Fourier formulation in favour of a boundary integral approach which proves especially effective in the strongly non-hydrostatic parameter range, including the regime of large-amplitude waves. Finally, this computational tool is applied to extend the critical overturning curve to strongly non-hydrostatic flows over Gaussian and bell-shaped ridges.

2. Long's theory

It is a quirk of the equations for an incompressible, inviscid and Boussinesq fluid that there are instances where the streamfunction $\psi(x, z)$ for time-steady disturbances satisfies the 2D linear Helmholtz equation (Raymond 1972; Wuertle *et al.* 1996)

$$\psi_{xx} + \psi_{zz} + \left(\frac{\mathscr{N}}{\mathscr{U}}\right)^2 \psi = 0. \tag{2.1}$$

The simplest case occurs when both the upstream wind, $\mathscr{U}$, and the Brünt–Vaisala frequency, $\mathscr{N}$, are taken to be constants (Laprise & Peltier 1989), although the question of the general background conditions under which this linearity accident ensues is discussed in Yih (1960). By incompressibility, the steady winds are defined in terms of a disturbance streamfunction

$$u(x, z) = \mathscr{U} + \psi_z, \quad w(x, z) = -\psi_x, \tag{2.2}$$

with quiescent upstream conditions, $\psi(-\infty, z) = 0$. Under this assumption of uniform upstream wind, the total streamfunction is thus given by $\Psi(x, z) = \mathscr{U}z + \psi(x, z)$. Since the topographic surface, $z = H(x)$, must also be a streamline of the flow, a zero total streamfunction condition can be applied at the lower boundary

$$\mathscr{U}H(x) + \psi(x, H(x)) = 0. \tag{2.3}$$

Finally, in an atmosphere that is unbounded above, a radiation condition must be satisfied which ensures that disturbances either decay, or correspond to waves carrying energy away from topographic obstacles. Such a boundary condition can be applied either by imposing maximal upstream decay as Lyra (1943), or by specifying proper far-field behaviour of the Fourier modes as Queney (1948). Early validations of these radiation conditions are discussed by Grubišić & Lewis (2004) within the historical context of the Sierra Wave project.

The environmental parameters define a lengthscale $\mathscr{U}/\mathscr{N}$ – which corresponds to the reciprocal of what is often referred to as the Scorer parameter (Lilly & Klemp 1979). Simple topographic profiles introduce at least two additional lengthscales: a horizontal scale $\mathscr{L}$ and a height scale $\mathscr{H}$. Within this minimal set of scales, the flow behaviour is parameterized by two dimensionless ratios

$$\mathscr{A} \equiv \frac{\mathscr{N}\mathscr{H}}{\mathscr{U}}, \quad \sigma \equiv \frac{\mathscr{U}}{\mathscr{N}\mathscr{L}}. \tag{2.4}$$

https://doi.org/10.1017/jfm.2011.187 Published online by Cambridge University Press

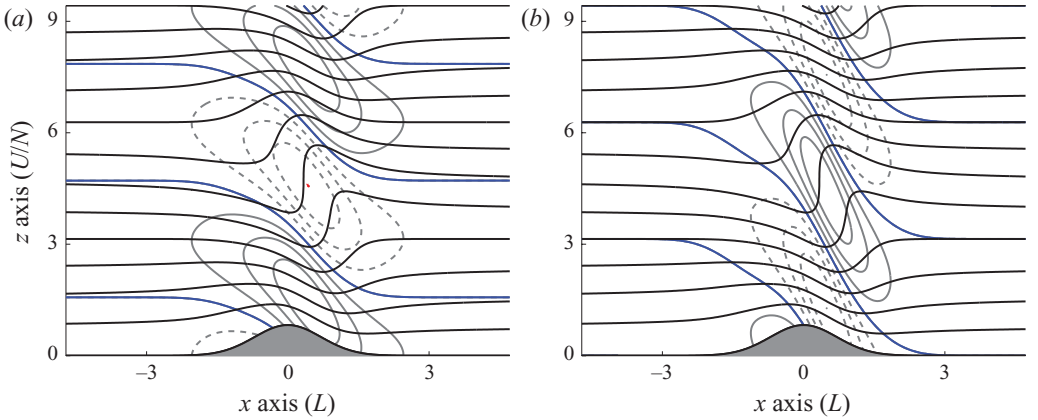


FIGURE 1. (Colour online available at journals.cambridge.org/FLM) Steady streamlines (dark) and disturbance velocities (light) contours for the hydrostatic limit ($\sigma = 0$) at critical overturning ($\mathscr{A}_c \approx 0.823$). Disturbance u-winds (a) and vertical motion w (b) are shown with negative values dashed. Contours are spaced at 0.25 of maximum disturbances ($|u|_{max} \approx 1.00\,\mathscr{U}$, $|w|_{max} \approx 1.40\,\sigma\mathscr{U}$).

The first, $\mathscr{A}$, is the height parameter which is of order 1 when the surface isentrope displacement is comparable to the vertical wavescale. The second, σ, is the non-hydrostatic parameter which primarily controls the downstream wavetrain. At the extreme of broad topography ($\sigma = 0$) is the hydrostatic limit. Such flows are characterized by the vertical wavescale $\mathscr{U}/\mathscr{N}$, but without any downstream dispersion of waves. At the other extreme of narrow topography ($\sigma > 1$) are strongly non-hydrostatic flows. In this case, despite the disparity between the topographic lengthscale and the horizontal wavescale, significant waves can still be generated when $\mathscr{A} = O(1)$.

Rescaling the horizontal coordinate on $\mathscr{L}$, the vertical coordinate on the wavescale $\mathscr{U}/\mathscr{N}$ and the streamfunction on $\mathscr{U}\mathscr{H}$ expresses the non-dimensional Long's theory (2.1) with its surface condition (2.3)

$$\sigma^2\psi_{xx} + \psi_{zz} + \psi = 0, \tag{2.5}$$

$$h(x) + \psi(x, \mathscr{A}\,h(x)) = 0, \tag{2.6}$$

in terms of the parameters $\mathscr{A}$ and σ. The topographic profile, $h(x)$, is normalized by maximum deviation ($\max|h(x)| = 1$), and is assumed to have no asymptotic height change: $h(-\infty) = h(+\infty) = 0$. The horizontal wind is scaled on $\mathscr{U}$, and the vertical motion on $\sigma\mathscr{U}$. It is clear that linear theory is obtained in the $\mathscr{A} = 0$ limit, as the evaluation of the surface boundary condition is displaced to $z = 0$. In addition, the choice of horizontal scale allows for a non-singular approach to the hydrostatic limit with $\sigma = 0$.

One of the characteristics of the steady wave flows is the tendency towards overturning streamlines with increased height topography (Smith 1977). Figure 1 shows the familiar case of critical overturning in a hydrostatic flow ($\sigma = 0$) past a Gaussian ridge. The minimum total u-wind is exactly zero and occurs where the streamline/isentope has a vertical slope. In general, the critical amplitude for the Gaussian ridge, $\mathscr{A}_c(\sigma)$, will depend on the non-hydrostatic parameter. Determining $\mathscr{A}_c(\sigma)$ requires calculating flow solutions over a range of $\mathscr{A}$ values and finding the smallest such value for which the minimum u-velocity is zero (the location of this

https://doi.org/10.1017/jfm.2011.187 Published online by Cambridge University Press

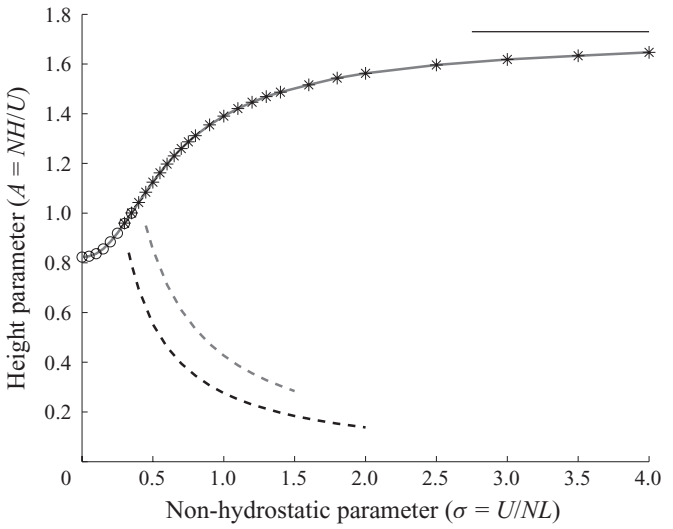


FIGURE 2. Critically overturning heights, $\mathscr{A}_c(\sigma)$, for Gaussian topography as a function of the non-hydrostatic parameter. Circles indicate values computed using the Fourier-based integral (3.4), while asterisks indicate cases computed using the boundary integral (5.6). The dashed curves show the degradation of the numerical conditioning of the Fourier-based solver, specifically indicating thresholds where seven (dark) and nine (light) digits are lost. The second-kind solver performs reliably for non-hydrostatic problems with $\sigma \geqslant 0.30$. A best-fit estimate of the upper asymptotic value of 1.73 is indicated by the dark thin line (7.2).

minimum must also be determined). This procedure for the hydrostatic example establishes $\mathscr{A}_c(0) \approx 0.823$, as shown in figure 1.

The repetitive nature of this zero-searching algorithm is assisted greatly by efficient and accurate numerical solvers. Based on the methods described in this paper, the curve of critical amplitudes has been calculated over a broad range of non-hydrostatic parameters (figure 2). In previous studies, only the critical regime for $\sigma \leqslant 0.5$ has been systematically explored (Laprise & Peltier 1989) using Fourier-based computations. Section 3 reviews the Fourier approach to Long's theory, and reveals it to be a purely linear computation. Section 4 then demonstrates its numerical ill-conditioning, especially for non-hydrostatic flows. This motivates the development, in §§ 5 and 6, of the boundary integral approach with which the strongly non-hydrostatic values of the curve of figure 2 were obtained.

3. The fourier method

The Fourier modes, $e^{i(kx+mz)}$, for the Helmholtz equation (2.5) satisfy the dispersion relation

$$m^2 = 1 - \sigma^2 k^2 \ , \tag{3.1}$$

where the sign choice of the vertical wavenumber $m(k)$ embodies the radiation condition. As determined by Lyra (1940), the appropriate choice is given by

$$m(k) = \begin{cases} \operatorname{sgn}(k)\sqrt{1-\sigma^2k^2} & \text{for } 0 < \sigma^2k^2 \leqslant 1, \\ \quad \mathrm{i}\,\sqrt{\sigma^2k^2-1} & \text{for } 1 \leqslant \sigma^2k^2 < \infty, \end{cases} \tag{3.2}$$

so that short waves decay with height, and propagating waves have upward group velocity. Waves just below the transition $\sigma k = 1$ have nearly horizontal group velocity,

https://doi.org/10.1017/jfm.2011.187 Published online by Cambridge University Press

so that the downstream far-field wake will be dominated by waves with horizontal wavelength $2\pi\sigma$ (thus $\mathscr{N}/\mathscr{U}$ is the natural downstream wavescale). The most general solution to the Helmholtz equation (2.5) that satisfies the radiation boundary condition has the Fourier representation

$$\psi(x,z) = -\int_{-\infty}^{+\infty} \hat{c}(k)\, \mathrm{e}^{\mathrm{i}(kx+m(k)z)}\, \mathrm{d}k \tag{3.3}$$

where $\hat{c}(k)$ is the complex-valued Fourier coefficient and is determined by the surface topography. Direct substitution into the surface boundary condition (2.6) gives

$$h(x) - \int_{-\infty}^{+\infty} \hat{c}(k)\, \mathrm{e}^{\mathrm{i}(kx+m(k)\mathscr{A}h(x))}\, \mathrm{d}k = 0. \tag{3.4}$$

This condition is a linear integral equation (Kondo 1991) for the unknown coefficient $\hat{c}(k)$ given the surface topography $h(x)$. Specifically, it is classified as an integral equation of a type known as a *Fredholm equation of the first kind*. Identifying the *kernel* function, $\mathscr{K}(x,k)$, as the exponential factor

$$\mathscr{K}(x,k) \equiv \mathrm{e}^{\mathrm{i}(kx+m(k)\mathscr{A}h(x))} \tag{3.5}$$

puts the surface condition (3.4) into the standard form (Wing 1991)

$$\int_{-\infty}^{+\infty} \mathscr{K}(x,k)\, \hat{c}(k)\, \mathrm{d}k = h(x)\ . \tag{3.6}$$

A key property of the left-side integral operator of (3.6) is that it acts linearly with respect to the unknown $\hat{c}(k)$. Therefore, even with the exact boundary condition (2.6), *the solution for Long's streamfunction is a purely linear problem.* This is not to be confused with the fact that the streamfunction, $\psi(x,z)$, as well as the Fourier coefficient $\hat{c}(k)$, depend nonlinearly on the topography $h(x)$ and the height parameter $\mathscr{A}$. Finally, in the limit of zero-height topography ($\mathscr{A} \to 0$), the integral in (3.6) is exactly a Fourier integral. The coefficient $\hat{c}(k)$ is then simply the Fourier transform of the topography

$$\hat{c}(k) \approx \frac{1}{2\pi} \int_{-\infty}^{+\infty} \mathrm{e}^{-\mathrm{i}kx}\, h(x)\, \mathrm{d}x = \hat{h}(k), \tag{3.7}$$

which recovers Lyra's linearized theory.

Although there exists extensive mathematical literature on the subject of linear integral equations, most of the attention is directed towards equations of the second kind. As discussed in Wing (1991), much of this is due to the fact that some key properties of first-kind equations make them poorly behaved relative to their second-kind cousin. The most debilitating of these is that first-kind integral operators generically have eigenvalues arbitrarily close to zero – and this has the severe consequence that computational solutions are guaranteed to become ill-conditioned with increased resolution. Nonetheless, in the next section, it is demonstrated that reliable solutions of Long's theory can be obtained from the integral equation as formulated in (3.6) over a limited range of parameter space.

4. The Fourier computations

The most straightforward computational approach for solving (3.6) is to approximate the integral by numerical quadrature over discrete wavenumbers k_m, for $-N \leqslant m \leqslant +N$, and unknowns $\hat{c}_m = \hat{c}(k_m)$. A determining set of $2N+1$ equations

https://doi.org/10.1017/jfm.2011.187 Published online by Cambridge University Press

for the unknown coefficients $\hat{c}_m$ is obtained by evaluating at $2N+1$ different spatial positions x_n, for $-N \leqslant n \leqslant +N$. At each x_n, such an approximation of (3.6) can be written as the summation

$$\sum_{m=-N}^{N} w_m \, \mathscr{K}(x_n, k_m) \, \hat{c}_m = h(x_n), \tag{4.1}$$

where w_m are the weights for the numerical quadrature (such as trapezoidal rule). Over all n, the result is a set of $2N+1$ linear equations for the $2N+1$ unknowns $\hat{c}_m$ whose form is that of a matrix equation

$$[\boldsymbol{K}]\, \boldsymbol{c} = \boldsymbol{h} \tag{4.2}$$

where $\boldsymbol{h} = (h_n)$ and $\boldsymbol{c} = (\hat{c}_m)$ are column vectors. The most straightforward implementation places the discretizations $k_m = m\Delta k$ and $x_n = n\Delta x$ onto uniformly spaced, and symmetric-about-zero grids. Further details are deferred to Appendix A.

This discretization of the integral (3.4) provides a direct (i.e., non-iterative) method for obtaining solutions to Long's theory. The example used here is the Gaussian topography

$$h(x) = \mathrm{e}^{-x^2}, \quad \hat{h}(k) = \frac{1}{2\sqrt{\pi}} \, \mathrm{e}^{-k^2/4}, \tag{4.3}$$

where $\hat{h}(k)$ denotes the Fourier transform. The hydrostatic ($\sigma = 0$) calculation shown in figure 1 is taken from a much wider computational domain of $-8\pi < x < 8\pi$ (with $\Delta x = \pi/32$ and $N = 255$). The additional width is necessary because the Fourier nature of the representation (3.3) allows for spurious wraparound of waves. The real and imaginary parts of the Fourier coefficient $\hat{c}(k)$ are shown in figure 3*a*. The real part (solid) differs only slightly from the Fourier transform of the topography $\hat{h}(k)$ (4.3). However, the imaginary part (dashed), which is exactly zero in linear theory (3.7), embodies the dominant effect due to the exact surface boundary condition (2.6).

Figure 4 shows the solution with the critical overturning of streamlines for the case of a weakly non-hydrostatic flow ($\sigma = 0.3$, $\mathscr{A}_c \approx 0.959$). With vertical inertia effects now included, a downstream wavetrain has appeared whose horizontal wavelength is roughly $2\pi\sigma$. An even wider computational domain $-32\pi < x < 32\pi$ (with $\Delta x = \pi/32$ and $N = 1023$) is now required so that upstream wraparound of this wavetrain is not evident in the plot domain. In both figures 1 and 4, the zero contours of velocity are shown as an indication of the suppression of upstream wave artefacts.

To achieve a similar accuracy (flow velocities converged to four significant digits with $\Delta x = \pi/32$) without upstream artefacts in the plot domain, the computational domain size increased by a factor of 4 between $\sigma = 0$ and $\sigma = 0.3$. Although this increase obviously affects the time and memory requirements for the computation, of more significant impact is that the linear problem (4.2) has become, in a relative sense, more singular. This is the ill-conditioning of the kernel matrix which manifests itself numerically through a sensitivity due to errors of finite-precision arithmetic. One measure of this problem is the log-condition number, which translates into a conservative estimate for the number of accurate digits lost by a linear solver (see Appendix A). The log-condition number increased from 2.90 for the hydrostatic case to 7.13 when $\sigma = 0.3$. Note especially that the Fourier coefficient $\hat{c}(k)$ for $\sigma = 0.3$ (figure 3*b*) displays little difference from the hydrostatic case, and gives no indication that this degradation of conditioning has occurred.

Thus, numerical ill-conditioning is the Achilles' heel for the Fourier-based method that restricts the accurate computation of large-amplitude solutions to those which are

https://doi.org/10.1017/jfm.2011.187 Published online by Cambridge University Press

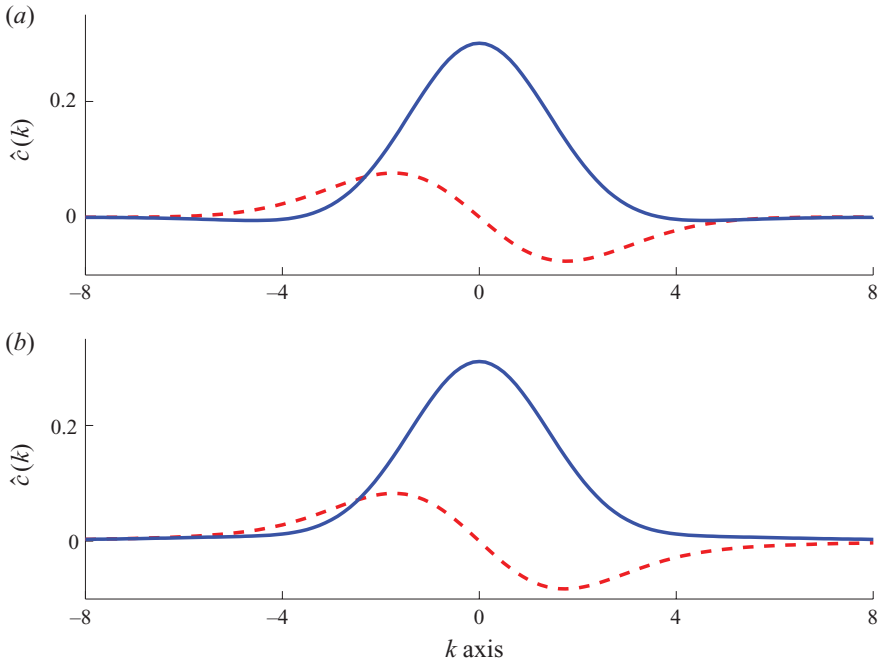


FIGURE 3. (Colour online) (*a*) Fourier coefficient $\hat{c}(k)$ for the hydrostatic flow ($\sigma = 0$) of figure 1. The real part (solid) differs only slightly from the Fourier transform of the topography $\hat{h}(k)$ (4.3). However, the imaginary part (dashed), which is exactly zero in linear theory, embodies the dominant effect due to the exact surface boundary condition (2.6). (*b*) Fourier coefficient for the non-hydrostatic flow ($\sigma = 0.3$) of figure 4. The only difference from the hydrostatic case is a very minor change in the decaying tails of the real part.

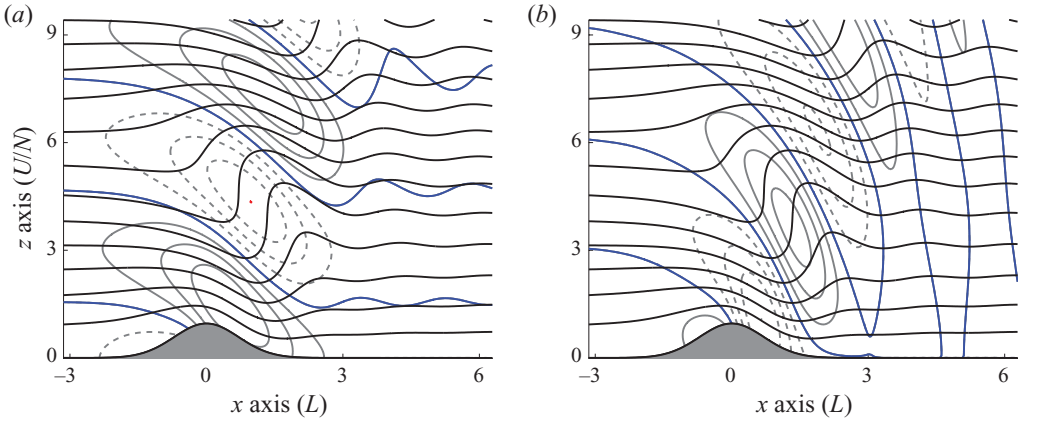


FIGURE 4. (Colour online) Steady streamlines (dark) and disturbance velocities (light) contours for a non-hydrostatic ($\sigma = 0.30$) case at critical overturning ($\mathscr{A}_c \approx 0.959$). Disturbance u-winds (*a*) and vertical motion w (*b*) are shown with negative values dashed. Contours are spaced at 0.25 of maximum disturbances ($|u|_{max} \approx 1.00\,\mathscr{U}$, $|w|_{max} \approx 1.57\,\sigma\mathscr{U}$). The downstream waves have a wavelength that is roughly $2\pi\sigma$.

weakly non-hydrostatic. Only those values of $\mathscr{A}_c(\sigma)$ marked by the circles in figure 2 (up to $\sigma = 0.35$) were computed here by Fourier means (3.4). The dark dashed curve of figure 2 indicates values in $(\sigma, \mathscr{A})$-parameter space where the log-condition number

https://doi.org/10.1017/jfm.2011.187 Published online by Cambridge University Press

of the kernel matrix reaches 7 (with $\Delta x = \pi/32$ and $N = 1023$). The light dashed curve indicates the threshold for a log-condition number of 9, at which point small gridscale oscillations are observed in the computed coefficients $\hat{c}(k)$. Although perhaps a conservative estimate on the (double-precision) computability of Long's solutions, these curves are consistent with the value of $\sigma = 0.5$ as the last data point in the Fourier-based calculations of Laprise & Peltier (1989). Note that it is the adoption of the Fourier representation that fundamentally leads to the ill-conditioning, as any choice of computational approach, whether direct or iterative, must still be solving (3.4). Hence, the computation of the values of $\mathscr{A}_c(\sigma)$ in figure 2 that are larger in the non-hydrostatic parameter $\sigma > 0.35$ necessitated a totally different mathematical approach. The boundary integral method, which overcomes the limitation inherent in the conditioning of the Fourier-based formulation, is described in the next section.

5. The boundary integral method

The Helmholtz equation (2.5) has long been studied for its application to the time-harmonic scattering of waves. In particular, there is well-established literature on linear integral equations and their computation via boundary integral methods. Based on mathematical potential theory, these methods presuppose knowledge of the appropriate Green's function (Green 1969). For many classical applications in electromagnetics or acoustics, the required Green's function is a Hankel (complex-valued Bessel) function. However, this result is specific for a far-field behaviour described by outgoing time-harmonic waves, and is not the same as the downstream wave condition of Lyra's linear theory. It is little known that the appropriate Green's function for the Helmholtz equation was derived by Lyra (1943) in the second of his original works.

For the non-hydrostatic case with $\sigma = 1$, Lyra's expression for the free-space Green's function is

$$\mathscr{G}(\boldsymbol{x}) = -\frac{1}{4}\, Y_0(r) - \frac{1}{\pi} \sum_{j=0}^{\infty} J_{2j+1}(r)\, \frac{\cos(2j+1)\phi}{2j+1}, \tag{5.1}$$

where $Y_0(r)$ and $J_n(r)$ are Bessel functions (Abramowitz & Stegun 1970). The polar coordinates (r, ϕ) are centred with the origin in the (x, z)-plane. This free-space Green's function satisfies the Helmholtz equation with a delta function forcing at the origin, without boundaries (i.e. free space). It is therefore a solution of Long's equation (2.5) everywhere but the origin, where it has a logarithmic singularity from the $Y_0(r)$ Bessel contribution. The series part is a non-singular contribution that was devised by Lyra (1943) to cancel the upstream waves.

Away from the singularity, the above Green's function (as does any of its derivatives and their translations) is a solution to the $\sigma = 1$ Helmholtz equation (2.5). The boundary integral method exploits this fact by representing the general Helmholtz solution as an integral superposition of Green's functions whose singularities lie along the topographic boundary. (Similar topographic use of the Green's function representation appears in Robinson (1969), and most recently revisited by Llewellen-Smith & Young (2003), for oceanic tidal flows over a barrier.) The boundary is defined by a (left-to-right) parameterization of the surface topography

$$\boldsymbol{\xi} \equiv \begin{pmatrix} \xi \\ \eta \end{pmatrix} = \begin{pmatrix} \xi \\ \mathscr{A} h(\xi) \end{pmatrix} \tag{5.2}$$

https://doi.org/10.1017/jfm.2011.187 Published online by Cambridge University Press

over $-\infty < \xi < +\infty$. The disturbance streamfunction is represented by an integral, along the boundary $\boldsymbol{\xi}$, that superimposes gradients of the Lyra Green's function

$$\psi(\boldsymbol{x}) = 2 \int_{\boldsymbol{\xi}} \mu(\xi)\, \frac{\partial \mathscr{G}}{\partial n}(\boldsymbol{x} - \boldsymbol{\xi})\, \mathrm{d}\xi, \tag{5.3}$$

where $\mu(\xi)$ is a density function to be determined by the surface condition (2.6). Since all singularities of the integrand lie on the surface, the integral (5.3) satisfies the Helmholtz equation (2.5) everywhere above the topography. Also, the far-field behaviour is inherited directly from the underlying Green's function; this underscores the importance of Lyra's solution (5.1) as the choice for $\mathscr{G}(\boldsymbol{x})$. The kernel is a normal derivative defined by

$$\frac{\partial \mathscr{G}}{\partial n} = \boldsymbol{n}(\xi) \cdot \begin{pmatrix} \mathscr{G}_\xi \\ \mathscr{G}_\eta \end{pmatrix} = \begin{pmatrix} \mathscr{A} h'(\xi) \\ -1 \end{pmatrix} \cdot \begin{pmatrix} \mathscr{G}_\xi \\ \mathscr{G}_\eta \end{pmatrix} \tag{5.4}$$

where $\boldsymbol{n}(\xi)$ is a normal vector into the topographic surface at $\boldsymbol{\xi}$. This representation for a Helmholtz solution is known as a double-layer potential (Green 1969), and it only remains to enforce the surface boundary condition (2.6).

Direct evaluation of the integral representation (5.3) is not possible for points on the surface topography

$$\boldsymbol{x}_s \equiv \begin{pmatrix} x \\ \mathscr{A} h(x) \end{pmatrix} \tag{5.5}$$

as the integrand involves the singularity of the Green's function at $\xi = x$. However, there is a classical limit for boundary points that resolves the double-layer formula into contributions from the local density, and the integral's principal value which deletes the singular point (Green 1969). Applying this textbook formula gives the surface version of (5.3)

$$-h(x) = -\mu(x) + 2 \fint_{\boldsymbol{\xi}} \mu(\xi)\, \frac{\partial \mathscr{G}}{\partial n}(\boldsymbol{x}_s - \boldsymbol{\xi})\, \mathrm{d}\xi, \tag{5.6}$$

where $\psi(\boldsymbol{x}_s) = -h(x)$ is taken from the boundary value (2.6). The result is a Fredholm integral equation for $\mu(\xi)$ that is of the desired *second-kind* variety (Wing 1991).

In the limit of zero-height topography ($\mathscr{A} = 0$), the boundary $\boldsymbol{\xi}$ flattens to the $\eta = 0$ axis, and the kernel (5.4) simplifies to $\partial \mathscr{G}/\partial n = \mathscr{G}_z(x - \xi, 0)$. The integral equation (5.6) becomes

$$-h(x) = -\mu(x) + 2 \fint_{-\infty}^{+\infty} \mu(\xi)\, \mathscr{G}_z(x - \xi, 0)\, \mathrm{d}\xi, \tag{5.7}$$

and since $\mathscr{G}_z(\xi, 0)$ is exactly zero in the principal value integral – the linear theory solution is simply $\mu(x) = h(x)$. The solution at interior points (5.3) then reduces to the convolution integral

$$\psi(x, z) = \int_{-\infty}^{+\infty} h(\xi)\, 2\mathscr{G}_z(x - \xi, z)\, \mathrm{d}\xi \tag{5.8}$$

and recovers Lyra's general solution to linear theory as was quoted in the English-language WMO Tech Report by Queney *et al.* (1960). The linear theory kernel, the z-derivative of (5.1), is given explicitly by

$$2\mathscr{G}_z(\boldsymbol{x}) = \frac{1}{2}\, Y_1(r)\, \sin\phi + \frac{2}{\pi} \sum_{j=1}^{\infty} J_{2j}(r)\, \frac{2j\, \sin 2j\phi}{4j^2 - 1}\,. \tag{5.9}$$

https://doi.org/10.1017/jfm.2011.187 Published online by Cambridge University Press

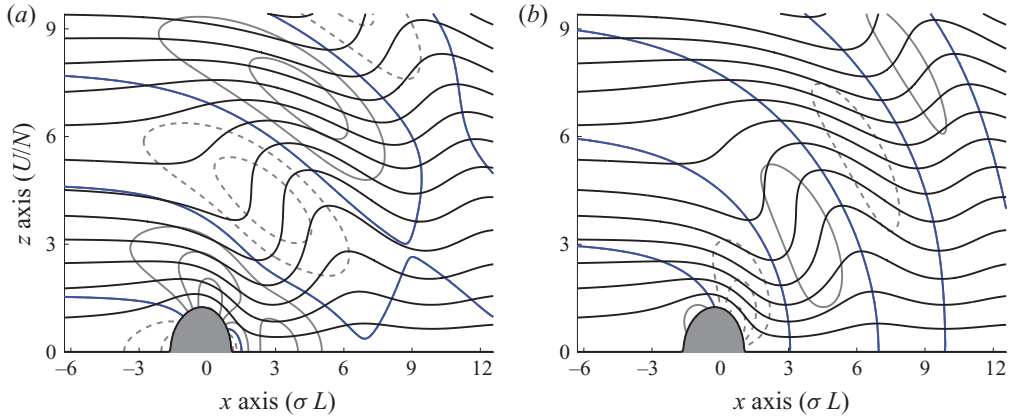


FIGURE 5. (Colour online) A critical overturning solution using Lyra's linear theory kernel (5.9). Streamlines (dark) and disturbance velocities (light) contours for the total streamfunction, $\Psi = z + 8.12\,\mathscr{G}_z(x, z)$. Disturbance u-winds shown in (a) and vertical motion w in (b) with negative contours dashed. Contours are spaced at 0.25 of maximum ($|u|_{max} \approx 1.52\,\mathscr{U}$; $|w|_{max} \approx 1.74\,\mathscr{U}$).

The generalization of the boundary integral formulas to $\sigma \neq 1$, which involve only rescalings of x, is summarized in Appendix B.

For topography that is a delta function at the origin, $h(x) = 4.06\,\delta(x)$, the (total) linear streamfunction is $\Psi = z + 8.12\,\mathscr{G}_z(x, z)$ – the significance of the factor of 4.06 corresponds to the $\sigma = 1$ critically overturning flow. A plot of the streamlines and contours of u and w is shown in figure 5. It is apparent that this flow also has the interpretation of a Long's solution, as the zero contour of streamfunction acts as a localized, dome-shaped obstacle. Although this flow strongly resembles the semi-circular flows of Kozhevnikov (1968) and Miles (1968), that it is not the same can be discerned by noting that the dome is displaced to the left of the origin. The cancellation of upstream waves is clearly evident. Following Appendix B, the case for $\sigma \neq 1$ merely requires a re-scaling of the horizontal axis $X = x/\sigma$. Thus, figure 5 represents a family of critically overturning flows for all non-hydrostatic values of σ, but for dome widths that scale on the wavescale $\mathscr{U}/\mathscr{N} = \sigma\mathscr{L}$. For this case, the vertical motion w does not scale on σ. In Appendix B, this special analytical solution assists in the computation of large-amplitude wave flows. The story behind this is discussed in the next section.

6. The boundary integral computations

Unlike the first-kind theory of § 3, the reformulation of Long's theory into a second-kind integral equation eliminates issues wtih numerical ill-conditioning (Wing 1991). The simplest computational approach to (5.6) is an approximation of the integral by numerical quadrature over discrete ξ_m, for $-N \leqslant m \leqslant +N$, and unknowns $\mu_m = \mu(\xi_m)$. A determining set of $2N + 1$ equations for the densities μ_m is obtained by evaluating at $2N + 1$ collocated positions $x_n = \xi_n$. Such a numerical discretization generically yields a well-conditioned linear problem as the $\mu(x)$-term outside of the integral (5.6) leads to a matrix that is diagonally dominant. Further details of the numerical implementation, including a subtlety associated with the principal value at the singular points (B 3), are deferred to Appendix B.

https://doi.org/10.1017/jfm.2011.187 Published online by Cambridge University Press

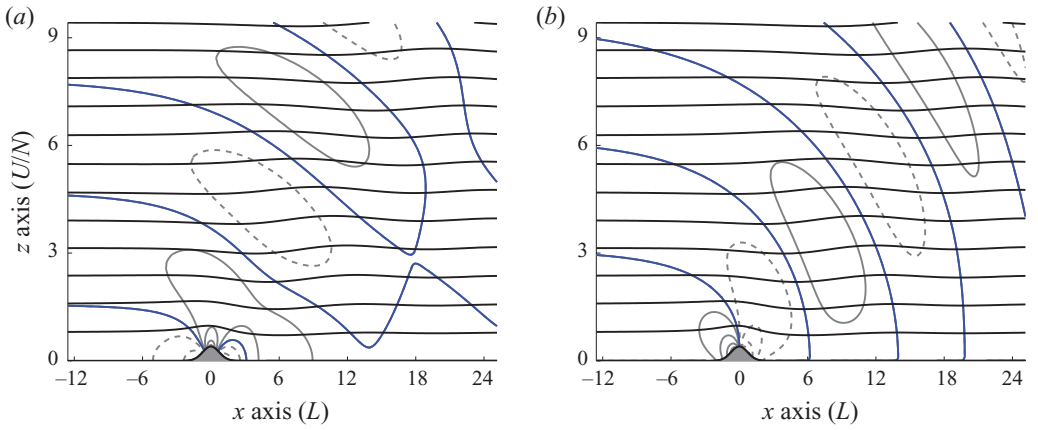


FIGURE 6. (Colour online) Steady streamlines (dark) and disturbance velocities (light) contours for a strongly non-hydrostatic ($\sigma = 2.0$) flow over a moderate height ridge ($\mathscr{A} = 0.4$). Disturbance u-winds (a) and vertical motion w (b) are shown with negative values dashed. Contours are spaced at 1/4 of maximum disturbances ($|u|_{max} \approx 0.84\,\mathscr{U}$, $|w|_{max} \approx 0.34\,\sigma\mathscr{U}$) with an extra contour to show the small-amplitude waves (1/12 in u, 1/16 in w). Note that the zero-velocity contours are essentially identical with those of figure 5.

Figure 6 shows a strongly non-hydrostatic solution for moderate height topography ($\sigma = 2.0$, $\mathscr{A} = 0.4$). This height is well below that required for critical overturning, The log-condition number of the linear solver is 1.01, although the flow parameters are just outside the computable region for the first-kind solver (figure 2). In contrast with Fourier methods, a solution based on Lyra Green's function (5.1) ensures that there cannot be upstream artefacts.

The flow of figure 6 consists of a slowly decaying train of downstream waves with horizontal wavelength $2\pi\sigma$. The $x^{-1/2}$ far-field dispersion of the waves matches both linear theory (Smith 1980), and the characteristic decay of the Bessel functions (Abramowitz & Stegun 1970). The far-field pattern of wavefronts, as suggested by the zero contours of u and w, coincide nearly with those of the linear theory kernel solution of figure 5.

Surface values for u and w are shown in figure 7, and is where the largest disturbance flows are found. The fastest u-disturbance ($u_{max} \approx 0.84\,\mathscr{U}$) is now found at the ridge summit; as opposed to an interior point as in figures 1 and 3. There is also considerable deceleration of the horizontal wind on the upstream ($u_{min} \approx -0.38\,\mathscr{U}$) and downstream lower slopes. The extremes of the vertical motion ($w_{max} \approx 0.34\,\sigma\mathscr{U}$; $w_{min} \approx -0.35\,\sigma\mathscr{U}$) are located on the ridge flanks.

Although the second-kind formulation has resolved the conditioning issue, two other serious numerical issues are encountered at higher, near-overturning heights. A foreshadowing of the first problem is seen in figure 8a, which shows the density $\mu(x/\sigma)$ relative to the Gaussian topography $h(x)$. Near the origin, $\mu(x/\sigma)$ is a slightly amplified version of the linear solution $h(x)$, but has a slow $x^{-1/2}$ decaying oscillation. For this moderate-amplitude case, capturing the tail requires a computational ξ-domain in excess of ± 100 (with $\Delta s = 0.05$ arclength spacing at the origin and $N = 512$) to obtain at least four-digit accuracy in interior velocities. As the obstacle height increases, so does the amplitude of this oscillatory tail. Maintaining accuracy of the flow solution, especially in the vicinity of the topography, requires larger downstream domains to correctly capture the tail of $\mu(x/\sigma)$. The second issue, and a

https://doi.org/10.1017/jfm.2011.187 Published online by Cambridge University Press

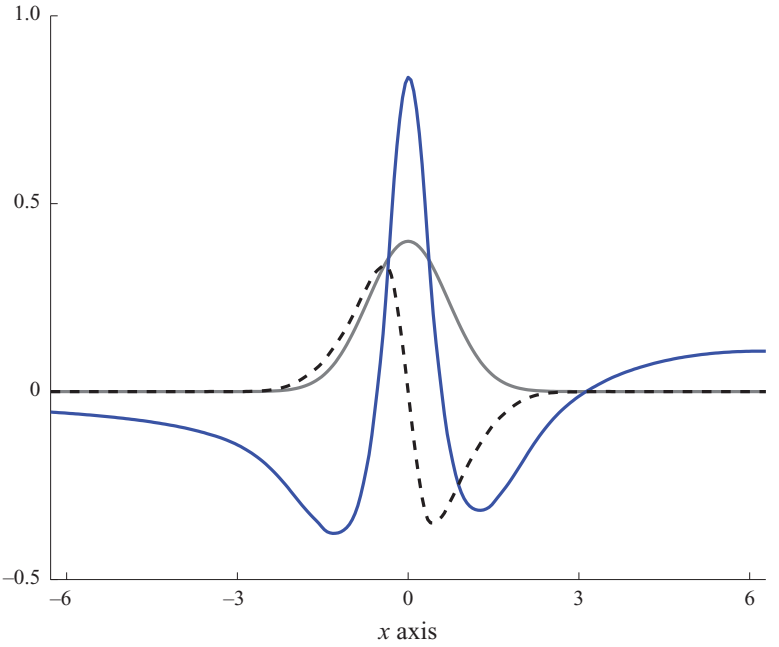


FIGURE 7. (Colour online) Surface values for the disturbance u-wind (dark solid) and vertical motion w (dark dashed) for the case of figure 6. Maximum disturbances are $|u|_{max} \approx 0.84\,\mathscr{U}$ and $|w|_{max} \approx 0.35\,\sigma\mathscr{U}$. The Gaussian topography $h(x)$ is indicated for reference (light solid).

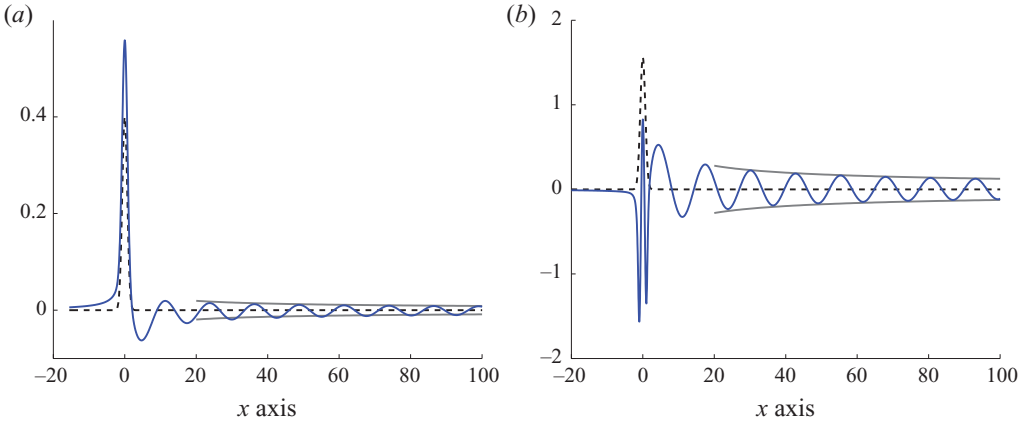


FIGURE 8. (Colour online) The computed density $\mu(x/\sigma)$ (dark solid, a) for the $\sigma = 2.0$ flow ($\mathscr{A} = 0.4$) of figure 6. The modified density $\mu^e(x/\sigma)$ (dark solid, b) is shown for the overturning flow ($\mathscr{A}_c \approx 1.562$) of figure 10. Note the change in vertical scale between (a) and (b). The oscillatory tails have wavelength $2\pi\sigma$ whose envelopes (light solid) decay as $x^{-1/2}$. The topographies, $h(x)$, are shown (dashed) for comparison. The $\mu(x/\sigma)$ in (a) is a perturbation of the topography $h(x)$, which is the $\mathscr{A} = 0$ solution. However, the $\mu^e(x/\sigma)$ in (b) mirrors the effective topography $h^e(x)$ (B 4).

much more serious one, is that calculating near-surface values and gradients of the boundary integral formula (5.3) is extremely problematic, due to kernel singularity. For surface winds, which require surface gradients, there is no analogue of the limit formula like that used to obtain (5.6). This is one of the fundamental drawbacks of

https://doi.org/10.1017/jfm.2011.187 Published online by Cambridge University Press

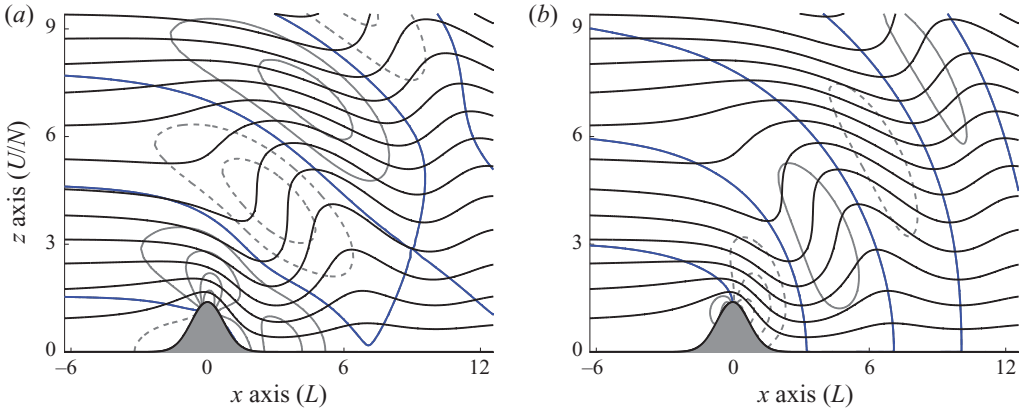


FIGURE 9. (Colour online) Steady streamlines (dark) and disturbance velocities (light) contours for a moderately non-hydrostatic ($\sigma = 1.0$) flow at critical overturning ($\mathscr{A}_c \approx 1.391$). Disturbance u-winds (a) and vertical motion w (b) are shown with negative values dashed. Contours are the same as figure 5 to illustrate the similarity of the far-field waves. Significant differences appear only in the vicinity of the topography.

boundary integral methods – far-field quantities are easily obtained to a high degree of accuracy, but near-surface values are not. The surface values shown in figure 7 have been obtained by careful extrapolation of near-surface values. An independent check on these surface values, $u_s(x)$ and $w_s(x)$, shows that the surface flow should follow the topography

$$w_s(x) - h'(x)\,(1 + \mathscr{A}\,u_s(x)) \;=\; 0, \tag{6.1}$$

and when applied to the curves of figure 7, reveals discrepancies as large as 0.02. This problem becomes more pronounced for large-amplitude wave flows so that accurate values of surface winds and pressures (and alas, pressure drag) for such flows as those of figure 2 cannot yet be included here.

There is, however, a resolution to the first problem, at least for the case of flow over a ridge. The basic idea is to exploit the linearity of the Helmholtz equation and the similarity of the downstream wavetrain (figure 6) with the Lyra linear kernel (figure 5). An enormous boost in effectiveness is gained by computing, not the entire solution, but only the difference from the linear theory kernel (5.9). This is how the critical overturning flow for $\sigma = 1.0$ ($\mathscr{A}_c \approx 1.391$) is computed. The streamlines are shown in figure 9 and, despite the difference in obstacle geometry, has a far-field that is nearly identical to the critical Lyra flow of figure 5. This is the last key idea needed to allow the extension of the critical curve of figure 2 into the region of strongly non-hydrostatic flows. The modification to the integral formulas for the difference computation (B 4) is outlined in Appendix B.

Figures 9 and 10 illustrate two of the critical values of figure 2 beyond the reach of traditional Fourier-based solvers ($\sigma = 1.0$, $\mathscr{A}_c \approx 1.391$ and $\sigma = 2.0$, $\mathscr{A}_c \approx 1.562$). The log-condition numbers for these linear problems were 2.47 and 2.80. Up to rescaling of x, the far-fields are well-anticipated by the linear theory kernel solution of figure 5. Both cases use common contour levels (four non-zero levels shown), but figure 10 would have a crush of u contours at the summit if more (equi-spaced) levels had been shown. To portray with reasonable accuracy both the far-field and the near-surface contours in figure 10, a computational ξ-domain in excess of ± 200 was used (with $\Delta s = 0.01$ arclength spacing at the origin and $N = 1024$).

https://doi.org/10.1017/jfm.2011.187 Published online by Cambridge University Press

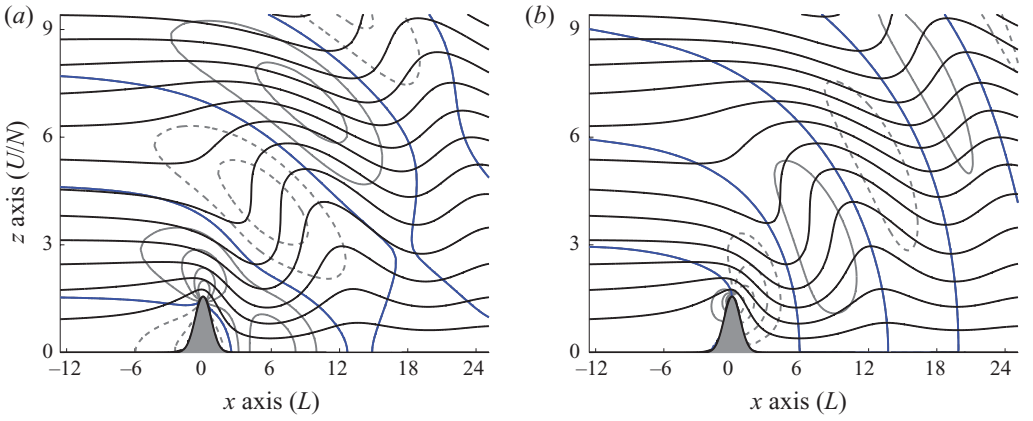


FIGURE 10. (Colour online) Steady streamlines (dark) and disturbance velocities (light) contours for a strongly non-hydrostatic ($\sigma = 2.0$) flow at critical overturning ($\mathscr{A}_c \approx 1.562$). Disturbance u-winds (a) and vertical motion w (b) are shown with negative values dashed. Contours are the same as figure 5 to illustrate the similarity of the far-field waves. There is no real difference with the flow of figure 9 except over the upslope and downslope of the topography.

Figure 8*b* shows the modified density $\mu^e(x/\sigma)$ for the flow of figure 10 based on a solution using the effective topography (B 4). The additional oscillations near the origin reflect the more complex structure of the effective topography $h^e(x)$. The amplitude of the oscillatory tail is still quite substantial in comparison to figure 8*a* except that $\mu^e(x/\sigma)$ is the density for only the difference from the Lyra flow.

7. Estimate of critical height asymptote

This implementation of a boundary integral method shows that the ill-conditioning problem which has limited previous computational studies of Long's theory can be overcome. The computation has been applied to extending the critical overturning curve (figure 2) as a function of the non-hydrostatic parameter. The results indicate that the critical value of height for overturning reaches an upper limit for large σ. A best-fit algebraic asymptote is calculated as

$$\mathscr{A}_c \sim (1.73) - (0.34)\sigma^{-0.99} \tag{7.1}$$

based on the values for $1 \leqslant \sigma \leqslant 4$ shown in figure 2. Accuracy issues in the zero-finding algorithm limit become problematic beyond $\sigma = 4$. It is noted that, while the quality of the fit curve supports the existence of the asymptote, the error criterion for the fit is fairly flat in the limiting value. So, the value of 1.73 could easily be shifted by a couple of percent, however, as the integral equation solver can be run with $\mathscr{A} = 1.73$ at larger σ (independently from the zero finding algorithm) – this appears to be a conservative estimate for an upper bound. This saturation of the critical height is consistent with the behaviour of the critical flow defined by the Lyra linear kernel (5.9). This flow has the special properties that it overturns for precisely the same height of dome for all values of σ, and has a far-field flow (which includes the overturning region) that is a good approximation of the Gaussian topographic flow at large σ.

The overturning analysis has also been carried out for the bell-shaped topography, $h(x) = 1/(1 + x^2)$. The critical overturning curve is shown in figure 11. A best-fit

https://doi.org/10.1017/jfm.2011.187 Published online by Cambridge University Press

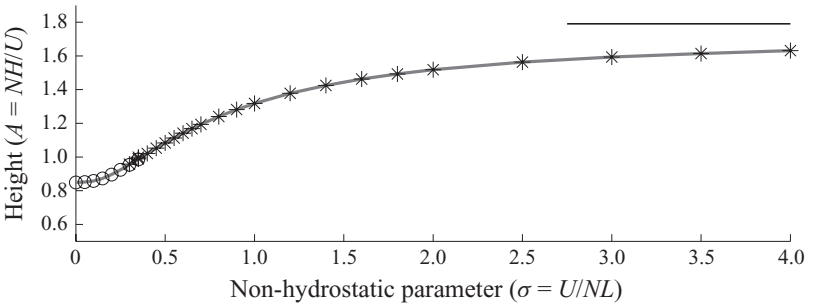


FIGURE 11. Critically overturning heights, $\mathscr{A}_c(\sigma)$, for bell-shaped topography as a function of the non-hydrostatic parameter. Circles indicate values computed using the Fourier-based integral equation (3.4), while asterisks indicate cases computed using the boundary integral equation (5.6). A best-fit estimate of the upper asymptotic value of 1.79 is indicated by the dark thin line (7.2).

algebraic asymptote is calculated as

$$\mathscr{A}_c \sim (1.79) - (0.47)\sigma^{-0.79} \tag{7.2}$$

based on the values for $1 \leqslant \sigma \leqslant 4$, and the similar caveats apply as noted for the Gaussian ridge.

8. In closing

It has been shown that Long's theory admits steady flow solutions up to overturning conditions for scales from the hydrostatic through the strongly non-hydrostatic regimes. In particular, the computational difficulties encountered for non-hydrostatic and large-amplitude flows are due to numerical ill-conditioning expected when solving first-kind integral equations. Here, the boundary integral method has been shown to perform well for moderate and strongly non-hydrostatic flows. Although the zero-finding algorithm seems to require extremely large discretizations to preserve accuracy beyond $\sigma \approx 4$, the integral equation solver alone (away from the surface) still performs at smaller amplitudes. However, by the singular nature of the Lyra Green's function at $\sigma = 0$, the boundary integral method is not useful for nearly hydrostatic flows. Hence, the Fourier and boundary integral methods are complementary approaches for computing Long's theory across the full range of parameters.

Although the Helmholtz equation is one of the standard textbook equations of mathematics, it should be noted that the issue of uniqueness of solution is still an area of active research for the geometry of a perturbed half-plane (Chandler-Wilde & Zhang 1999). Non-uniqueness would arise in the form of a non-zero solution to (5.6) with a zero on the left-side of the equation. Such a solution would indicate a resonance, and in a numerical computation would generate a near-singular matrix (for reasons distinct from the ill-conditioning of first-kind integral equations). The current state of mathematical proof suggests that there should be no problems for sufficiently small topography, and no such near-singularity was encountered in this study. Nonetheless, the possibility of resonance cannot be ruled out for more severe topographic profiles.

The boundary integral method presented here allows for the robust and accurate computation of the far-field flow for parameter values previously unattainable. Computations using this method, for a four-peaked obstacle, were used as an inviscid

https://doi.org/10.1017/jfm.2011.187 Published online by Cambridge University Press

baseline for interpreting the laboratory experiments in Aguilar *et al.* (2006). The computed Long's solution demonstrated that, while the experimental parameters for the case of the highest topography corresponded to a severely overturning flow, viscous effects were sufficient to suppress the appearance of wave turbulence. Typical of the non-hydrostatic and nonlinear regime is a large-amplitude wave response with an extended downstream wavetrain. The extremal u and w occur on the topographic surface, but have not yet been accurately computed. It is a quirk of the mathematics of potential theory that, despite the ignorance of the near-field details, the far-field flow can be computed with great accuracy. This inability to address surface conditions constitutes a serious weakness which will hopefully be remedied by future insights. The flows of figures 9 and 10 were computed via the difference from the Lyra Green's function. While this finesse works for upward topographic profiles, it is useless for deep valley flows since the Green's function is singular at the origin which is part of the flow domain. Adapting techniques for cavity geometries for depression topography is one direction for future consideration.

The latter part of this work would not have been realized without the inspiration from J. Klemp, who alerted the author to the WMO reference of the Lyra Green's function. Access to the original German language articles of Lyra were graciously made available by V. Grubišić and J. Kuettner. This work benefitted enormously from many discussions with L. Greengard, B. Alpert and A. Dienstfrey on the practical issues of accurately computing integral equations. The author also acknowledges the thoughtful and careful readings of the reviewers. The early development of the Fourier solver was part of the Master's thesis of D. Alexander (2004). This research was supported through NSERC RGPIN-238928.

Appendix A. The fourier implementation

Using trapezoidal rule for the quadrature approximation of (3.6) by (4.1), the elements of the matrix $\boldsymbol{K}$ are given by

$$\boldsymbol{K}_{nm} = \Delta k \begin{cases} \dfrac{\mathscr{K}(x_n, 0^+) + \mathscr{K}(x_n, 0^-)}{2}, & \text{for } m = 0, \\ \dfrac{\mathscr{K}(x_n, k_{-N})}{2}, & \text{for } m = -N, \\ \dfrac{\mathscr{K}(x_n, k_N)}{2}, & \text{for } m = +N, \\ \mathscr{K}(x_n, k_m), & \text{otherwise,} \end{cases} \tag{A 1}$$

where the weights of the quadrature are generically $w_m = \Delta k$ with exceptions at the endpoints where the contribution is halved. Special care must be taken at $k = 0$, since it represents a point of discontinuity of the kernel function (3.5). The appropriate value of $\boldsymbol{k}_0 = 0$ matrix elements is the average of the $\mathscr{K}(x, 0^+)$ and $\mathscr{K}(x, 0^-)$ limits. Once the coefficients $\hat{c}_m$ are obtained from the linear solution of (4.2), the streamfunction evaluation at any interior point (x, z)

$$\psi(x, z) = -\sum_{m=-N}^{N} w_m \, \mathrm{e}^{\mathrm{i}(k_m x + m(k_m) z)} \, \hat{c}_m \tag{A 2}$$

is a matrix multiply. The (non-dimensional) flow velocities ($u = 1 + \psi_z$ and $w = -\psi_x$) are calculated using the differentiations of (A 2).

https://doi.org/10.1017/jfm.2011.187 Published online by Cambridge University Press

With uniform discretizations, it is also essential that the product of $\Delta k\,\Delta x$ satisfy the condition

$$\Delta k\,\Delta x = \frac{\pi}{N+1} \tag{A 3}$$

in order for the matrix solution (4.2) to be computationally tractable. This is again the issue of numerical conditioning (Trefethen & Bau 1997), which is the susceptibility of numerical solutions of large linear systems to the accumulation of round-off errors. The base-10 logarithm of the matrix condition number gives a rough indication of the number of digits lost due to finite-precision round-off (out of 16 digits in double-precision arithmetic). As an indication of the sensitivity in this matrix conditioning, a 2% change in the product $\Delta k\,\Delta x$ in either direction from (A 3) leads to a potential digit loss in excess of 17, and thus renders a double-precision numerical solution meaningless. This condition on $\Delta k\,\Delta x$ derives from the fact that for $\mathscr{A}=0$, the integral equation (3.4) is a Fourier transform and is an exceptional case that is perfectly conditioned. With (A 3), the kernel matrix (3.5) for $\mathscr{A}=0$ is then very nearly the perfectly conditioned discrete Fourier matrix. For finite, nonzero values of $\mathscr{A}$, the conditioning degrades but not so much as to prevent numerical solution of (3.6) up to the critical overturning in the hydrostatic case of figure 1. This is distinct from the loss of conditioning with respect to increasing the non-hydrostatic parameter σ which is the subject of § 4.

Appendix B. The boundary integral implementation

Generalizing the integral formulas for $\sigma\neq 1$ requires only that the horizontal coordinate be scaled on the wavescale $\mathscr{U}/\mathscr{N}$ instead of $\mathscr{L}$. In terms of $X=x/\sigma$, the disturbance streamfunction, $\psi(X,z)$, satisfies the $\sigma=1$ Helmholtz equation and permits the use of the Lyra Green's function $\mathscr{G}(X,z)$. For $\sigma\neq 1$, the equation for the density (5.6) becomes

$$-h(\sigma X) = -\mu(X) + 2\fint_{\xi} \mu(\xi)\,\frac{\partial \mathscr{G}}{\partial n}(\boldsymbol{X}_s-\boldsymbol{\xi})\,\mathrm{d}\xi, \tag{B 1}$$

where the surface parameterization and normal derivative are defined with respect to the (X,z) coordinates. Then, the integral representation (5.3) of the solution in (X,z) coordinates becomes

$$\psi(X,z) = 2\int_{\xi} \mu(\xi)\,\frac{\partial \mathscr{G}}{\partial n}(\boldsymbol{X}-\boldsymbol{\xi})\,\mathrm{d}\xi \tag{B 2}$$

from which the horizontal wind $u(X,z)=\psi_z(X,z)$ and vertical motion $w(X,z)=-\psi_X(X,z)/\sigma$ are obtained. All quantities are plotted on axes in terms of the x values.

The quadrature points ξ_m for the integral in (5.6) or (B 1) need not be uniformly spaced. Near the ridge, uniform spacing in arclength (Δs) is found to work well; while for the far-field downstream, 10–12 points per wavelength proves adequate. Trapezoidal rule is used for the quadrature. With the collocated discretizations, $x_n=\xi_n$, the diagonal elements of the quadrature matrix from (5.6) are evaluations at the singularity of the Lyra kernel (5.4). An advantage of the double-layer potential formulation is that the Lyra kernel has a finite (l'Hôpital) limit as the contour approaches the singularity point

$$\lim_{\boldsymbol{\xi}\to\boldsymbol{X}_s} \frac{\partial \mathscr{G}}{\partial n}(\boldsymbol{X}_s-\boldsymbol{\xi}) = -\frac{1}{4\pi R}, \tag{B 3}$$

where R is the radius of curvature of the contour $\boldsymbol{\xi}$ in (X,z) coordinates.

https://doi.org/10.1017/jfm.2011.187 Published online by Cambridge University Press

For the critical overturning computations, considerable reduction of the oscillatory tail (by a factor of roughly 5 for figure 8) is obtained by computing only the difference from the Lyra kernel solution (figure 5). The only change is the replacement of $h(x/\sigma)$ the left-side of (B 1) by an effective topography

$$h^e(\sigma X) = h(\sigma X) - (8.12)\,\mathscr{G}_z(X, \mathscr{A}h(\sigma X)) \ . \tag{B 4}$$

Finally, as with the Fourier method of § 3, the choice of plot points is completely independent of the quadrature points which are used to determine $\mu(X)$. The numerical evaluation of boundary integrals, once $\mu(X)$ is known, is quite accurate away from the boundary contour – in particular, the overturning points. Note that it is far more accurate to evaluate the velocities u and w by integrating the derivative kernel of (5.3) instead of finite-differencing the streamfunction.

Near the surface, the boundary integral methods require special treatment. One simple approach for computing values close to (and on) the boundary, is to use an interpolation of the $\mu(X)$ onto a denser discretization (say, a factor of 10). Gridded values for contouring are then obtained by interpolation or extrapolation of near-surface values.

REFERENCES

Abramowitz, M. & Stegun, I. A. 1970 *Handbook of Mathematical Functions*. National Bureau of Standards.

Aguilar, D. A., Sutherland, B. R. & Muraki, D. J. 2006 Laboratory generation of internal waves from sinusoidal topography. *Deep-Sea Res.* II **53**, 96–115.

Alexander, D. E. 2004 *Stability of Steady, Stratified Flow over Two-Dimensional Topography*. Masters thesis. Simon Fraser University.

Brown, D. J. & Christie, D. R. 1998 Fully nonlinear solitary waves in continuously stratified incompressible Boussinesq fluids. *Phys. Fluids* **10**, 2569–2586.

Chandler-Wilde, S. N., Ross, C. R. & Zhang, B. 1999 Scattering by infinite one-dimensional rough surfaces. *Proc. R. Soc.* A **455**, 3767–3787.

Drazin, P. G. & Su, C. H. 1975 A note on long-wave theory of airflow over a mountain. *J. Atmos. Sci.* **32**, 437–439.

Dubreil-Jacotin, M.-L. 1932 Sur les ondes de type permanent dans les liquides hétérogènes. *Atti della R. Acc. Naz. dei Lincei* **15**, 814–819.

Dubreil-Jacotin, M.-L. 1935 Complément à une note antérieure sur les ondes de type permanent dans les liquides hétérogènes. *Atti della R. Acc. Naz. dei Lincei* **21**, 344–346.

Dubreil-Jacotin, M.-L. 1937 Sur les théoremes d'existence relatifs aux ondes permanentes périodiques à deux dimensions dans les liquides hétérogènes. *J. Math. Pures Appl.* **16**, 43–67.

Durran, D. R. 1992 Two-layer solutions to Long's equation for vertically propagating mountain waves: How good is linear theory? *Quart. J. Roy. Meteor. Soc.* **118**, 415–433.

Green, C. D. 1969 *Integral Equation Methods*. Barnes & Noble.

Grubišić, V. & Lewis, J. M. 2004 Sierra wave project revisited. *BAMS* **8**, 1127–1142.

Kantzios, Y. D. & Akylas, T. R. 1993 An asymptotic theory of nonlinear stratified flow of large depth over topography. *Proc. R. Soc. Lond.* A **440**, 639–653.

Kondo, J. 1991 *Integral Equations*. Oxford University Press.

Kozhevnikov, V. N. 1968 Orographic perturbations in the two-dimensional stationary problem. *Atmos. Ocean. Phys. (Izv. Akad. nauk SSSR, Fiz. atmos. okeana)* **4**, 16–27.

Laprise, R. & Peltier, W. R. 1989 On the structural characteristics of steady finite-amplitude mountain waves over bell-shaped topography. *J. Atmos. Sci.* **46** (4), 1498–1529.

Lilly, D. K. & Klemp, J. B. 1979 The effects of terrain shape on nonlinear hydrostatic mountain waves. *J. Fluid. Mech.* **95**(2), 241–261.

Llewellen-Smith, S. G. & Young, W. R. 2003 Tidal conversion at a very steep ridge. *J. Fluid Mech.* **495**, 175–191.

https://doi.org/10.1017/jfm.2011.187 Published online by Cambridge University Press

Long, R. R. 1953 Some aspects of the flow of stratifed fluids. i. A theoretical investigation. *Tellus* **5**(1), 42–58.

Long, R. R. 1955 Some aspects of the flow of stratifed fluids. iii. Continuous density gradients. *Tellus* **7**(3), 341–357.

Lyra, G. 1940 Über den Einfluß von Bodenerhebungen auf die Strömung einer stabil geschichteten Atmosphäre. *Beitr. Phys. Freien Atmos.* **26**, 197–206.

Lyra, G. 1943 Theorie der stationären Leewellenströmung in freier Atmosphäre. *Z. Angew. Math. Mech.* **28**, 1–28.

Miles, J. W. 1968 Lee waves in a stratified flow. Part 2. Semi-circular obstacle. *J. Fluid Mech.* **33** (4), 803–814.

Miles, J. W. & Huppert, H. E. 1969 Lee waves in a stratified flow. Part 4. Perturbation approximations. *J. Fluid Mech.* **35**(3), 497–525.

Queney, P. 1948 The problem of air flow over mountains: A summary of theoretical results. *Bull. Am. Meteor. Soc.* **29**, 16–26.

Queney, P., Corby, G. A., Gerbier, N., Koschmieder, H. & Zierep, J. 1960 The airflow over mountains. *Tech. Rep.* 34. World Meteorological Organization, Geneva, Switzerland.

Raymond, D. J. 1972 Calculation of airflow over an arbitrary ridge including diabatic heating and cooling. *J. Atmos. Sci.* **29**, 837–843.

Robinson, R. M. 1969 The effects of a barrier on internal waves. *Deep-Sea Res.* **16**, 421–429.

Scorer, R. S. 1949 Theory of waves in the lee of mountains. *Q. J. R. Meteorol. Soc.* **75**, 41–56.

Smith, R. B. 1977 The steepening of hydrostatic mountain waves. *J. Atmos. Sci.* **34**, 1634–1654.

Smith, R. B. 1979 The influence of mountains on the atmosphere. In *Advances in Geophysics*, vol. 21, pp. 87–230. Elsevier.

Smith, R. B. 1980 Linear theory of stratified hydrostatic flow past an isolated mountain. *Tellus*, vol. 32, pp. 348–364.

Trefethen, L. N. & Bau, D. 1997 *Numerical Linear Algebra*. SIAM.

Wing, G. M. 1991 *A Primer on Integral Equations of the First Kind*. SIAM.

Wuertle, M. G., Sharman, R. D. & Datta, A. 1996 Atmospheric lee waves. *Annu. Rev. Fluid Mech.* **28**, 429–476.

Yih, C.-S. 1960 Exact solutions for steady two-dimensional flow of a stratified fluid. *J. Fluid Mech.* **9**, 161–174.

https://doi.org/10.1017/jfm.2011.187 Published online by Cambridge University Press